

# Selective CO<sub>2</sub> reduction to acetate via controlled *sp*<sup>2</sup>/*sp*<sup>3</sup> carbon hybridization

Received: 20 February 2025

Accepted: 16 October 2025

Published online: 25 November 2025



Chujun Wang<sup>1,2,3,4,5,9</sup>, Gong Zhang<sup>1,2,9</sup>, Ran Luo<sup>1,2,3,4,5,6</sup>, Yixian Wang<sup>1,2,3,4,5</sup>, Xiao Ma<sup>1,2,3,4,5</sup>, Mengmeng Zhang<sup>1,2</sup>, Xin Chang<sup>1,2,3,4,5,6</sup>, Zhi-Jian Zhao<sup>1,2,4,5</sup> ✉, Tuo Wang<sup>1,2,3,4,5</sup> ✉ & Jinlong Gong<sup>1,2,5,7,8</sup> ✉

Electrocatalytic reduction of CO<sub>2</sub> to fuels and chemicals represents a promising pathway for CO<sub>2</sub> utilization and energy conversion. However, metal-based catalysts often suffer from diminished selectivity in the direct reduction of CO<sub>2</sub> to acetate due to suboptimal intermediate adsorption energy imposed by the linear scaling relationship of *d*-band theory. We describe a deposition-etching strategy that tunes the *sp*<sup>2</sup>/*sp*<sup>3</sup> hybridization of carbon in diamond to tune the adsorption equilibrium of intermediates for CO<sub>2</sub> reduction to acetate, which circumvents the constraints of the *d*-band electrons. This metal-free catalyst achieves a Faradaic efficiency of 62.7% for CO<sub>2</sub>-to-acetate conversion and demonstrated 100 hours durability. Mechanistic studies reveal that introducing *sp*<sup>2</sup>-carbons into the *sp*<sup>3</sup>-carbon matrix can control the adsorption energies of \*CO<sub>2</sub> and \*CO. The *sp*<sup>2</sup>/*sp*<sup>3</sup>-carbon active sites facilitate the formation of the \*CHO intermediate, which is asymmetrically coupled with the \*CO<sub>I</sub> to generate acetate.

The electrochemical CO<sub>2</sub> reduction reaction (CO<sub>2</sub>RR) driven by renewable electricity provides a pathway for long-term energy storage<sup>1–3</sup>. To date, the energy efficiency toward C<sub>1</sub> (e.g. CO and HCOOH)<sup>4,5</sup> and some C<sub>2+</sub> products (e.g. C<sub>2</sub>H<sub>4</sub> and alcohol)<sup>6,7</sup> of electrochemical CO<sub>2</sub>RR have approached the threshold of commercial viability, while the efficiency and selectivity of acetate are still far from satisfactory<sup>8,9</sup>. Compared to ethylene and ethanol, acetate has a higher degree of asymmetry and a lower degree of protonation, making the adsorption equilibrium of key intermediates more challenging<sup>10–12</sup>. However, with metal catalysts, it is difficult to attain the adsorption equilibrium of key intermediates due to the scaling relationship of adsorbent (especially \*COOH, \*CO, \*CHO, and \*H)<sup>13–15</sup>. Furthermore, multi-component metallic catalysts often encounter challenges such as surface segregation, reconstruction, and elemental leaching, thus limiting long-term stability<sup>16</sup>.

Unlike metallic elements, carbon atoms in carbon materials bind intermediates through outer *p*-orbitals, exhibiting different adsorption properties distinct from *d*-band metals<sup>17,18</sup>. Among them, diamond has gained significant attention due to its excellent properties, such as long-term durability, inertness of hydrogen evolution, different dimensionalities from 0 to three dimensional (3D) with various shapes, and environmental friendliness<sup>19</sup>. In reported works, diamonds have demonstrated unique acetate selectivity, which benefits from the electronic tunability at the heterogeneous interface or N doping<sup>20,21</sup>. However, the pristine boron-doped diamond (BDD) electrode can only reduce CO<sub>2</sub> to formic acid due to its weak bonding strength to CO<sub>2</sub><sup>22,23</sup>. Therefore, an additional component is required to polarize the *sp*<sup>3</sup>-carbon (*sp*<sup>3</sup>-C) in the diamond phase, promoting CO<sub>2</sub> adsorption and regulating the adsorption equilibrium of intermediates. As another hybrid form of carbon,

<sup>1</sup>School of Chemical Engineering & Technology, Key Laboratory for Green Chemical Technology of Ministry of Education, Tianjin University, Tianjin 300072, China. <sup>2</sup>Collaborative Innovation Center for Chemical Science & Engineering (Tianjin), Tianjin 300072, China. <sup>3</sup>National Industry-Education Platform of Energy Storage, Tianjin University, 135 Yaguan Road, Tianjin 300350, China. <sup>4</sup>Haihe Laboratory of Sustainable Chemical Transformations, Tianjin 300192, China. <sup>5</sup>International Joint Laboratory of Low-carbon Chemical Engineering of Ministry of Education, Tianjin 300192, China. <sup>6</sup>Joint School of National University of Singapore and Tianjin University, International Campus of Tianjin University, Binhai New City, Fuzhou 350207, China. <sup>7</sup>Tianjin Normal University, Tianjin 300387, China. <sup>8</sup>State Key Laboratory of Synthetic Biology, Tianjin University, Tianjin 300072, China. <sup>9</sup>These authors contributed equally: Chujun Wang, Gong Zhang. ✉e-mail: [zjzhao@tju.edu.cn](mailto:zjzhao@tju.edu.cn); [wangtuo@tju.edu.cn](mailto:wangtuo@tju.edu.cn); [jlgong@tju.edu.cn](mailto:jlgong@tju.edu.cn)

$sp^2$ -carbon ( $sp^2$ -C) exhibits a different electronic structure, and unbonded single electrons or electron clouds formed after  $\pi$ - $\pi$  conjugation will affect the electronic structure of neighboring atoms<sup>24</sup>. Introducing  $sp^2$ -C to the diamond surface and constructing the heterostructure of  $sp^3$ -C and  $sp^2$ -C might modulate the electronic structure of  $sp^3$ -C<sup>25,26</sup>. In addition, the asymmetric sites composed of  $sp^2$ -C and  $sp^3$ -C will also be favorable for the formation of asymmetric products<sup>12,27</sup>. However, there lacks a methodology to precisely control the structure and proportional balance between  $sp^2$ -C and  $sp^3$ -C, which is fundamental for modulating the electronic structure and adsorption property at the heterogeneous interface, a critical factor for the conversion of  $CO_2$  into acetate. Conventional synthesis methods, such as organic synthesis, solvothermal/hydrothermal synthesis, etc.<sup>28</sup>, fall short in simultaneously achieving a heterostructure that integrates  $sp^3$ -C and  $sp^2$ -C, a high-density of active sites, and flexible adjustment of  $sp^2$ -C content.

Herein, we present the design and implementation of a deposition-etching strategy to tune the  $sp^2/sp^3$  hybridization carbon structure in BDD electrodes, aimed at enhancing  $CO_2$  reduction to acetate. This method enables the creation of a high density of  $sp^3$  carbon with dangling bonds as active sites and modulates the amount of modified  $sp^2$  hybrid carbon groups. The adsorption equilibrium of the reaction intermediates could be achieved by modulating the proportion of  $sp^2$ -C and  $sp^3$ -C, which breaks the linear scaling relationship of the  $d$ -band theory for metal sites. The asymmetric structure, composed of  $sp^2$ -C and  $sp^3$ -C, adsorbs \*CO intermediates in two different forms, which leads to different degrees of protonation and asymmetric  $C_2$  intermediates, ultimately inducing the formation of acetate. Remarkably, a Faradaic efficiency of 62.7% for  $CO_2$ -to-acetate conversion, as the exclusive  $C_{2+}$  product, was achieved with a high current density of  $23\text{ mA cm}^{-2}$  on a metal-free catalyst. Additionally, this catalyst exhibits exceptional durability, maintaining its activity for up to 100 h with a minimal decline rate of  $0.12\% \text{ h}^{-1}$ . This performance surpasses previously reported performances of non-metallic electrocatalysts to date, establishing a benchmark in the field.

## Results

### Controlled regulation of $sp^2$ -C and $sp^3$ -C heterostructure

The commercially available as-deposited polycrystalline BDD films were grown on silicon (100) substrate by microwave plasma-assisted chemical vapor deposition (MPCVD)<sup>22</sup>. The boron concentration in the commercial BDD film is determined by the boron-to-carbon ratio (B/C) in the precursor gas mixture, corresponding to a 1:1000 molar ratio of trimethylboron (boron source) to methane (carbon source), and is maintained at 0.1% for boron doping (details in Methods). Following MPCVD, we constructed the diamond nanocones on the BDD by an inductively coupled plasma-reactive ion etching (ICP-RIE) method (Fig. 1a and Supplementary Fig. 1, details in Methods). This etching technology combines chemical etching reactions with physical bombardment etching, which enables high etch rates with high etch selectivity, as well as low surface damage<sup>29,30</sup>. Chemical etching reactions are based on the reaction of free radicals with the surface of the etched material, which produces volatile species that desorb from the surface. Physical etching, on the other hand, relies on high-energy ion bombardment and knockout of atoms or aggregates of atoms in the etched material. Modulating the independent ICP and capacitive coupled plasma (CCP) etching power during the etching process can synergistically achieve different fluxes of energetic ions in the chamber (Supplementary Fig. 2), leading to the cleavage of carbon-carbon bonds of the substrate, which may partially transform part of the  $sp^3$  carbon ( $sp^3$ -C) structure in the material into the  $sp^2$  carbon ( $sp^2$ -C) structure. Based on this hypothesis, we obtained three typical etched BDD electrodes with different  $sp^2/sp^3$  hybridization carbon structures by etching powers (details in Methods), i.e., low ion flux, medium ion flux, and high ion flux etched BDDs (referred to as  $E_L$ BDD,  $E_M$ BDD, and

$E_H$ BDD, respectively). The structural composition of the hybridized carbon in BDD electrodes may be affected by the aforementioned processes.

To explore the effect of different ion fluxes on the morphology and the composition of obtained BDDs, scanning electron microscope (SEM) and spherical aberration-corrected transmission electron microscopy (AC-TEM) were applied. The commercial BDD electrodes initially show flat microcrystalline diamond polyhedrons (Supplementary Fig. 3). After etching with medium ion flux, the surface of  $E_M$ BDD exhibits uniformly sized and well-aligned nanocone arrays with sharp tips (Fig. 1b). Further increasing etching power (i.e., high ion flux), the  $E_H$ BDD surface underwent erosion by ion bombardment, resulting in blurred grain boundaries (Supplementary Fig. 4). To further investigate the fine structure of diamond nanocones, ultra-thin specimens of  $E_M$ BDD were fabricated by focused ion beam (FIB) technique for cross-sectional TEM analysis (Supplementary Fig. 5 and Methods). Cross-sectional AC-TEM image of the bulk region of the nanocone and the selected area electron diffraction (SAED) pattern indicates its  $\langle 111 \rangle$  growth orientation<sup>29,30</sup> (Fig. 1c). Meanwhile, high-resolution TEM (HRTEM, Fig. 1d) showed atomic structures transitioning from ordered arrays in the bulk to continuous crooked lines near the surface, suggesting a breakdown into  $sp^2$ -C or graphene layers<sup>31</sup> (The dashed rectangular frame in Fig. 1d). This breakdown can be attributed to the lack of the support of three-dimensional structures, resulting in the neighboring graphene layers or  $sp^2$ -C chains making contact with each other and bending with flexibility<sup>32</sup>. Therefore, the  $sp^3$ -to- $sp^2$  carbon transition is clearly observed in the HRTEM images of  $E_M$ BDD, evidenced by the presence of compressed graphitic carbon layers inserted within and bonded at high angles to  $sp^3$ -bonded diamond surfaces. In contrast, the unetched BDD exhibits a highly ordered HRTEM lattice corresponding to the diamond structure from the bulk to the surface (Supplementary Fig. 6a). Furthermore, after heavy etching ( $E_H$ BDD), more  $sp^2$ -C was generated and converted into graphite layers covering the diamond surface (Supplementary Fig. 6c), which may not favor the  $CO_2$ RR. As the interface advances to the diamond side, the specifically combined structural motifs impose constraints on the carbon bonds in adjacent diamond, resulting in significant stacking disorder of carbon structure in the diamond<sup>32</sup>. This structural arrangement indicates a topotaxial relationship between the two domain types, demonstrating that the etched BDD forms a transformation from diamond to graphite. Upon etching, the surface morphology of the BDD electrode was altered, and the degree of phase transformation and the content of  $sp^2$  hybridized carbon on the electrode surface could be finely controlled by modification of the ion flux during the etching process, which is expected to bring about changes in the distribution of  $CO_2$ RR products.

To further illustrate the structural transformation upon etching, we used electron energy loss spectroscopy (EELS) to identify the distribution of  $sp^2$  and  $sp^3$  carbons (Fig. 1f). In the aberration-corrected high-angle dark-field scanning transmission electron microscopy (HAADF-STEM) image of  $E_M$ BDD (Fig. 1e), the EELS scanning paths are marked with blue arrows, with positions 1-6 corresponding to distances of 1-6 nm from the surface (Fig. 1f). The EELS spectra at positions 3-6 exhibit  $sp^3$ - $\sigma^*$  antibonding states characteristic of the diamond, whereas positions 1-3 indicate the coexistence of both  $sp^2$  and  $sp^3$  bonded carbons<sup>33</sup>. The peak near 285 eV corresponds to electronic transitions from 1s core states to unoccupied  $\pi^*$  ( $2p_z$ ) states of  $sp^2$ -C<sup>34</sup>. Further, corresponding multiple linear least squares (MLLS) quantitative analysis<sup>35</sup> reveals the contributions of  $sp^2$  and  $sp^3$  bonded carbons at each position (Fig. 1g). For  $E_M$ BDD, the  $sp^2$ -C content is highest at the surface and position 1 region, where  $sp^2$ -bonded graphitic domains are prominently visible within the dashed rectangular frame of the HRTEM images (Fig. 1d). In contrast, the  $sp^2$  content on the surface of  $E_L$ BDD is nearly negligible (Supplementary Fig. 7c). In comparison the surface of  $E_H$ BDD shows significantly higher  $sp^2$

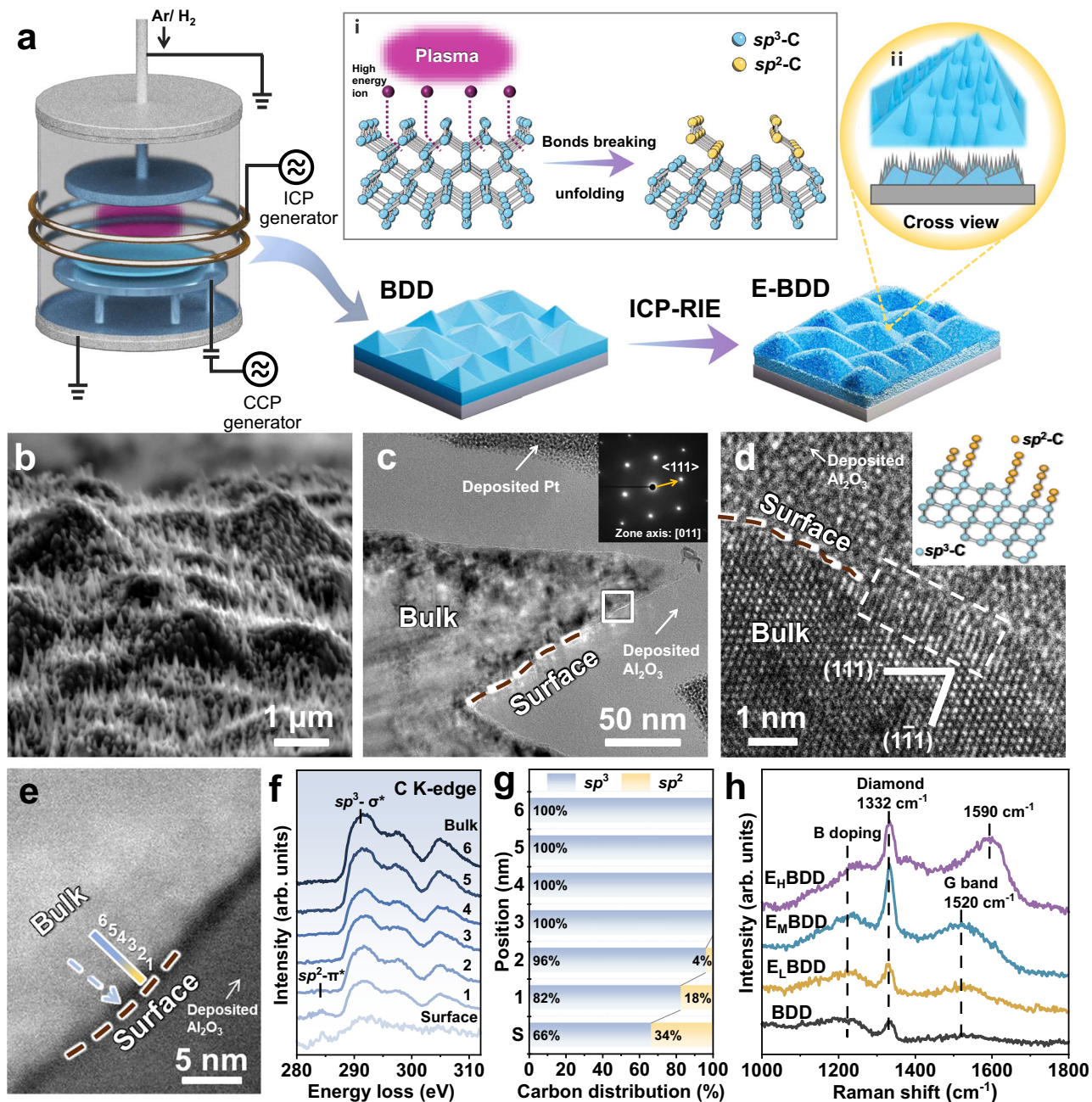


**Fig. 1 | Preparation and structural characterization of E-BDD film electrodes.**

**a** Schematic preparation process of E-BDD film electrode. Inset i, mechanism schematic of the BDD film ICP-RIE process. Atom code:  $sp^3$ -C, blue;  $sp^2$ -C, yellow. Inset ii, enlarged cross-view of E-BDD film. **b** SEM image of  $E_M$ BDD film. **c** Cross-sectional AC-TEM of the nanocone of  $E_M$ BDD with the inserted selected area electron diffraction (SAED) pattern (The dark red dashed lines are used to distinguish the surface of the nanocone. A  $Al_2O_3$  protective layer was deposited before FIB processes and a Pt protective layer was deposited during the FIB thinning process). **d** Cross-sectional HRTEM images of the nanocone of  $E_M$ BDD (the capture area is

marked by the rectangle in (c)). Inset, the corresponding atomic models of a covalently bonded  $sp^2$ -C and  $sp^3$ -C heterostructure, with adjacent carbon layers distinctly shaded in varying greyscales for clarity. **e** Cross-sectional HAADF-STEM image of the nanocone of  $E_M$ BDD (the capture area is marked by the rectangle in (c)). **f** The EELS spectra of C K-edge. The line scan direction and acquisition position are marked by the blue arrow and numbers in (e). **g** Percentage distribution of  $sp^2$  and  $sp^3$  by the MLLS quantitative analysis for (f)  $E_M$ BDD. **h** Raman spectra of BDD and E-BDD films. Source data are provided as a Source Data file.

content, with a small amount of  $sp^2$  persisting up to 4 nm from the surface (Supplementary Fig. 8c), which aligns well with the previous HRTEM observations (Supplementary Fig. 6). The presence of a certain amount of  $sp^3$  bonded carbons neighboring the surface of E-BDDs suggests that the  $sp^2$  bonded structure does not form a continuous layer, such as the structure observed in onion-like carbon<sup>36</sup>. Rather, it is dispersed and forms a heterogeneous structure with  $sp^3$  carbon. This suggests that the changes of the ion flux have the potential to alter the coverage and distribution depth of  $sp^2$ -C on the surface of E-BDDs.

In order to further confirm these findings, the grazing incidence X-ray diffraction (GIXRD) was performed (Supplementary Fig. 9). In addition to peaks from pristine BDD, the E-BDDs exhibit diffraction peaks assignable to hexagonal graphite (HG)<sup>32</sup> a characteristic transition phase between diamond and graphite. This structural evolution aligns with HRTEM observations. Excessive etching in the  $E_H$ BDD reveals a distinct, broad peak characteristic of amorphous carbon. The formation of surface  $sp^2$ -C may be initiated by the cleavage of robust  $sp^3$  bonds during etching from energetic ions. Subsequently, these

broken hexagonal crystal cells unfold and transform into a two-dimensional graphite structure that remains coherently connected to the diamond lattice via covalent C–C bonds<sup>30,31,34</sup> (Fig. 1a Inset i). Ultimately, the above process leads to the accumulation of  $sp^2$ -C on the  $E_{\text{H}}\text{BDD}$  surface.

To link the variation of the  $sp^2/sp^3$  ratio with etching power, we further performed Raman and X-ray photoelectron spectroscopy (XPS). The Raman spectra of BDD and E-BDDs exhibit sharp peaks at 1332  $\text{cm}^{-1}$  of the zone center phonon line (ZCP) of the diamond<sup>19</sup> (Fig. 1h). The broadband formation at 1220  $\text{cm}^{-1}$  is attributed to boron doping<sup>23</sup>. During the etching process, boron-doped defects are more easily etched, resulting in more prominent ZCP peaks for E-BDD electrodes than for BDD electrodes, indicating a higher quality diamond phase<sup>22</sup>. The G band observed between 1500–1600  $\text{cm}^{-1}$  arises from the bond stretching of  $sp^2$ -C atoms present in both rings and chains<sup>24</sup>. Initially, the unetched BDD electrode exhibits a negligible G-band intensity, indicating minimal presence of  $sp^2$ -C. With an increase in etching power, there is a gradual enhancement in the intensity of the G band, suggesting that the diamond surface structure disrupted by etching transformed into  $sp^2$ -C. Under higher etching power ( $E_{\text{H}}\text{BDD}$ ), more  $sp^2$ -C was generated and converted into a more ordered graphite phase structure, leading to a blue shift of the G-band (1590  $\text{cm}^{-1}$ ) along with the weakening of the ZCP peak<sup>32</sup>. Similarly, C 1s spectra show that the content of  $sp^2$ -C increased gradually with the etching power<sup>22</sup> (Supplementary Fig. 10). It's worth noting that only carbon and small amounts of adsorbed oxygen were detected by the XPS and energy dispersive spectroscopy (EDS) (Supplementary Figs. 11 and 12).

In summary, the structural and compositional changes of E-BDD due to different etching ion fluxes have been confirmed from multiple perspectives. The shift in the G-band peak position in Raman spectroscopy suggests the presence of various types of  $sp^2$ -C in E-BDDs. Specifically, high ion flux  $E_{\text{H}}\text{BDD}$  forms a graphite overlayer, while low and medium ion flux E-BDDs contain a mixture of amorphous carbon and graphite. Consequently, the ICP-RIE strategy enables varied  $sp^2$ -C proportions on  $sp^3$ -C surfaces, exposing more active sites and potentially altering  $\text{CO}_2\text{RR}$  product distribution.

### Effect of $sp^2$ -C and $sp^3$ -C heterostructure on $\text{CO}_2$ electroreduction performance

We evaluated the  $\text{CO}_2$  reduction performance of unetched BDD and E-BDDs in an H-type cell (H-cell) with  $\text{CO}_2$ -saturated 0.1 M  $\text{KHCO}_3$  as the catholyte (Supplementary Fig. 13). Polarization ( $j$ -V) curves indicate significantly higher current densities for E-BDD electrodes compared to unetched BDD, may be due to enhanced electron transfer rate (Supplementary Fig. 14) and  $\text{CO}_2$  reduction activity (Supplementary Fig. 15). Further, we carried out the chronoamperometry measurements, and the gas and liquid products were detected using online gas chromatography and  $^1\text{H}$ -nuclear magnetic resonance ( $^1\text{H}$ -NMR) spectrometer, respectively (Supplementary Figs. 16 and 17). The major  $\text{CO}_2$  reduction product of unetched BDD is formate ( $\text{HCOO}^-$ ) which exhibits a Faradaic efficiency (FE) of 51.8% at  $-1.6$  V *vs.* RHE (Supplementary Fig. 18a). After the low degree of etching,  $E_{\text{L}}\text{BDD}$  shows obvious changes in product selectivity that CO (37.3% FE at  $-1.5$  V *vs.* RHE) replaces  $\text{HCOO}^-$  (22.9% FE at  $-1.5$  V *vs.* RHE) as the major product of  $\text{CO}_2$  reduction (Supplementary Fig. 18b). The strength and adsorption configuration of  $^*\text{CO}_2^-$  intermediate bind to the catalyst surface determines the production of  $\text{HCOO}^-$  and CO, with the former requiring a weaker binding force and the latter requiring a stronger one<sup>22,23,37</sup>. Hence, the presence of CO in  $E_{\text{L}}\text{BDD}$  demonstrates that adding a small quantity of  $sp^2$ -C can enhance the binding energy of the intermediate. More interestingly, we detected small amount of acetate in the liquid phase (8.2% FE at  $-1.5$  V *vs.* RHE). This prompted us to suspect that a higher proportion of  $sp^2$ -C might further enhance the activity for acetate formation. Exactly, with greater  $sp^2$ -C content,  $E_{\text{M}}\text{BDD}$  achieves the maximum FE of acetate ( $\text{CH}_3\text{COO}^-$ , 33.5% FE at

$-1.5$  V *vs.* RHE) with a total current density of 15  $\text{mA cm}^{-2}$  (Fig. 2a) and the FE of CO decreased markedly from 37.3% to 23.7% (Supplementary Fig. 19a). However, under heavy etching conditions, the  $\text{CO}_2$  reduction efficiency of  $E_{\text{H}}\text{BDD}$  decreases significantly ( $\text{CH}_3\text{COO}^-$  10.2% FE and CO 16.3% FE at  $-1.5$  V *vs.* RHE), and HER dominated ( $\text{H}_2$ , 61.3% FE at  $-1.5$  V *vs.* RHE) (Supplementary Figs. 18c and 19). This may be attributed to the fact that the entire surface of the  $sp^3$ -C structure is covered with excess  $sp^2$ -C, which is favorable for HER over  $\text{CO}_2\text{RR}$ <sup>38,39</sup>. Therefore, the introduction of  $sp^2$ -C can improve the adsorption properties of the  $sp^3$ -C structure. The pure  $sp^3$ -C structure can only convert  $\text{CO}_2$  into  $\text{HCOO}^-$  due to its weak  $\text{CO}_2$  binding ability<sup>33</sup>, but excessive  $sp^2$ -C would accelerate  $\text{H}_2$  production (Fig. 2b). Only an appropriate proportion of  $sp^2$ -C can balance adsorption properties, allowing more  $^*\text{CO}$  and other  $\text{C}_1$  intermediates to be retained and coupled to yield  $\text{CH}_3\text{COO}^-$  (Supplementary Figs. 19 and 20). These results confirm the potential for adjusting the adsorption equilibrium of reaction intermediates by tuning the  $sp^2/sp^3$ -C proportion, indicating that  $p$ -region elements serving as catalytic sites break the linear relationship of metal sites.

To reveal the changes in intrinsic catalytic activity and electrochemical properties induced by etching, the electrochemically active surface area (ECSA) of BDD and E-BDD electrodes was measured (Supplementary Figs. 21). The ECSA increases gradually with the increased etching power, indicating that more active sites are exposed after etching. After calculating the current density normalized by ECSA,  $E_{\text{M}}\text{BDD}$  still exhibits the highest acetate current density, indicating that its intrinsic activity is indeed enhanced, which may correspond to a possible change in the acetate generation pathway (Supplementary Fig. 22).

We recognize that the low solubility of  $\text{CO}_2$  in the H-cell may limit the activity of our prepared E-BDD electrodes. We propose further surface modification of the electrodes to enhance the local  $\text{CO}_2$  concentration (see below for detailed analysis). Inspired by previous reports<sup>40,41</sup> and considering the Lewis acidity of  $\text{CO}_2$ , we suggest using basic amino groups for surface functionalization. As expected, a significant enhancement in the FE of acetate was observed upon the introduction of amino groups onto the  $E_{\text{M}}\text{BDD}$  surface ( $E_{\text{M}}\text{BDD-NH}_2$ ). This modification was achieved through electroreduction amination<sup>40,42</sup> (details in Methods and Supplementary Figs. 23 and 24), with the carbon structure of  $E_{\text{M}}\text{BDD-NH}_2$  remaining unchanged relative to  $E_{\text{M}}\text{BDD}$  (Supplementary Figs. 25–27). For  $E_{\text{M}}\text{BDD-NH}_2$ , the introduction of the amino group significantly increased the current density of  $E_{\text{M}}\text{BDD-NH}_2$  compared to the unmodified counterpart (Supplementary Fig. 28) and led to a reduction in the competing hydrogen evolution reaction. The FE of  $\text{CH}_3\text{COO}^-$  reached 62.7% at  $-1.5$  V *vs.* RHE with a total current density of 23  $\text{mA cm}^{-2}$  (Fig. 2c) and the ECSA shows no significant increase (Supplementary Fig. 29). Compared to  $E_{\text{M}}\text{BDD}$ , the FE of acetate showed an overall improvement with a 1.9-fold increase at the optimal potential (Supplementary Fig. 30). To elucidate the function of the amino group, both BDD electrode and graphite electrode were also modified with the amino group. Despite these modifications, the product distribution remained unchanged, with no acetate detected (Supplementary Fig. 31), reaffirming the heterostructure composed of  $sp^2$ -C and  $sp^3$ -C is crucial for acetate production.

Given that carbon-based materials are employed as electrodes, it is essential to trace the origin of the carbon present in the products. First, trace analysis using inductively coupled plasma mass spectrometry (ICP-MS) verified the absence of detectable metal impurities in both the electrode and the testing system, ruling out the possibility of catalytic effect from metal impurities (Supplementary Table 1). Next, we employed  $^{13}\text{CO}_2$  as raw gas for isotope labeling experiments on  $E_{\text{M}}\text{BDD}$  and  $E_{\text{M}}\text{BDD-NH}_2$ . Liquid products in electrolytes were analyzed by  $^1\text{H}$ -NMR and mass spectrometry (MS) confirmed that the carbon in acetate originated from  $^{13}\text{CO}_2$  (Supplementary Figs. 32–35). The FE for acetate production under  $^{13}\text{CO}_2$  labeling conditions was 60.4%, closely matching the value of 62.7% determined under unlabeled  $\text{CO}_2$  at

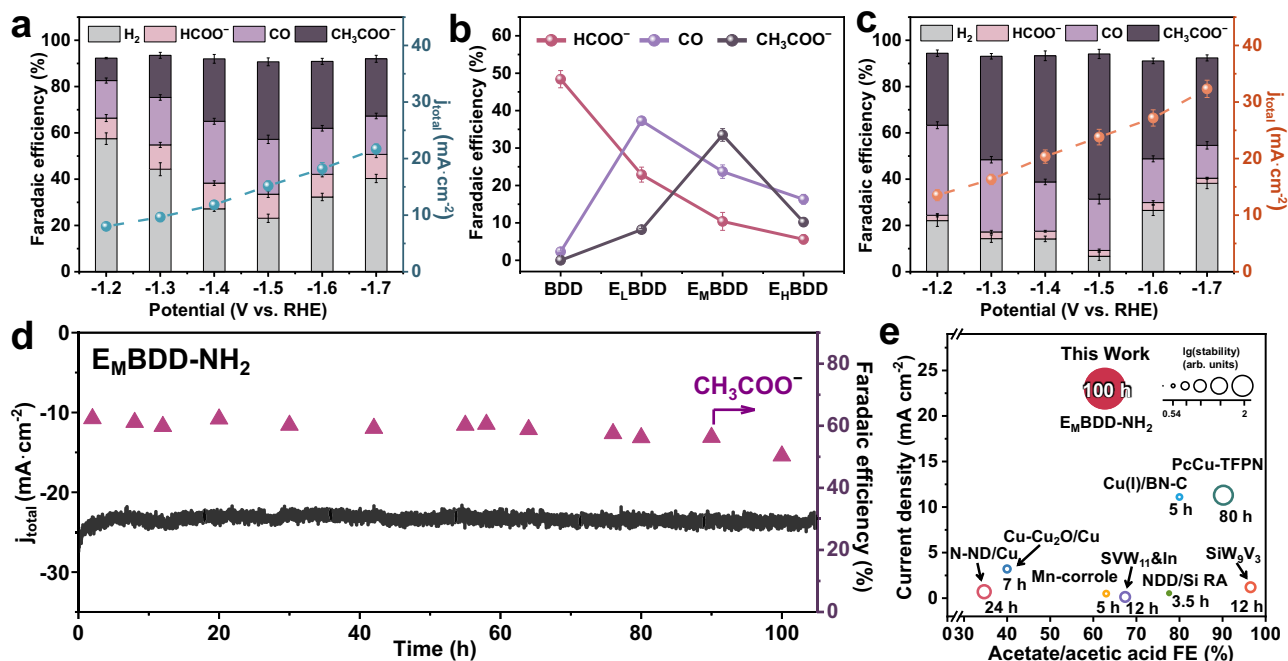


**Fig. 2 | Electrochemical CO<sub>2</sub>RR performances.** **a** Product distribution afforded by E<sub>M</sub>BDD after 3 h CO<sub>2</sub>RR. **b** CO<sub>2</sub>RR product selectivity (FE, %) productions on BDD, E<sub>1</sub>BDD, E<sub>M</sub>BDD, and E<sub>H</sub>BDD at the potential of -1.5 V *vs.* RHE after 3 h reaction. **c** Product distribution afforded by E<sub>M</sub>BDD-NH<sub>2</sub> after 3 h CO<sub>2</sub>RR. **d** Current density-time (*j*-*t*) curves of E<sub>M</sub>BDD-NH<sub>2</sub> under the temporal evolution at the potential of -1.5 V *vs.* RHE for 100 h. **e** Comparison of the acetate/acetic acid FE, current density, and stability in CO<sub>2</sub>RR between E<sub>M</sub>BDD-NH<sub>2</sub> in this work and the state-of-the-art

catalysts in the literature (see Supplementary Table 2 for details), where the bubble scale represents the logarithm of stability (h) to the base of 10. All electrochemical tests were conducted in a CO<sub>2</sub>-saturated 0.1 M KHCO<sub>3</sub> (pH = 6.81) electrolyte solution at room temperature (25 °C) without iR compensation. Error bars represent the standard deviation from at least three independent measurements. Source data are provided as a Source Data file.

identical potentials. The results confirmed that the carbon of the acetate product was derived from CO<sub>2</sub>. No acetate was detected in the absence of CO<sub>2</sub>, catalyst, or applied potential (Supplementary Fig. 36).

Durability of E<sub>M</sub>BDD-NH<sub>2</sub> toward CH<sub>3</sub>COO<sup>-</sup> electro-synthesis was also assessed, with the final FE remaining above 50% after 100 h of continuous electrolysis (Fig. 2d). Post-reaction analysis shows no significant changes in topography and crystal structure of E<sub>M</sub>BDD-NH<sub>2</sub> (Supplementary Fig. 37). Meanwhile, XPS analysis confirms the unchanged carbon hybridization structures and integrity of surface amino groups (Supplementary Fig. 38).

The FE of CH<sub>3</sub>COO<sup>-</sup>, current density, and stability were further compared with those reported previously (Fig. 2e and Supplementary Table 2). E<sub>M</sub>BDD-NH<sub>2</sub> demonstrates a higher FE for acetate than the majority of catalysts reported thus far (with some catalysts exhibiting FEs below 50%) along with a higher CO<sub>2</sub>RR current density of 23 mA cm<sup>-2</sup>. Acetate as the sole C<sub>2+</sub> liquid-phase product significantly reduces the costs of subsequent separation processes. Moreover, thanks to its stable diamond structure, the use of E<sub>M</sub>BDD-NH<sub>2</sub> reduces the frequency of electrode replacement during continuous acetate production, thereby helping to lower operational costs.

Overall, E<sub>M</sub>BDD-NH<sub>2</sub> exhibits notable long-term stability and electroreduction performance for CO<sub>2</sub> conversion into acetate. To the best of our knowledge, few studies can achieve such long-term stability for the CO<sub>2</sub>RR to acetate products at an acetate partial current density of exceeding 14 mA cm<sup>-2</sup>. Therefore, the present E<sub>M</sub>BDD-NH<sub>2</sub> demonstrates great promise for the direct conversion of CO<sub>2</sub> into acetate products, especially when utilizing a non-metal catalyst.

### The formation mechanism of acetate on *sp*<sup>2</sup>-C and *sp*<sup>3</sup>-C heterostructure

As a heterogeneous catalytic process, strong CO<sub>2</sub> binding is typically regarded as a crucial stage for CO<sub>2</sub> reduction. To understand the

mechanism that the CO<sub>2</sub> reduction products changed after etching, we conducted CO<sub>2</sub> temperature-programmed desorption (CO<sub>2</sub>-TPD) on unetched BDD and E-BDDs (Fig. 3a). Due to the differences in specific surface area among the unetched BDD and E-BDDs, the CO<sub>2</sub> binding strength was assessed by the desorption temperature rather than the desorption amount. The unetched BDD surface possesses negligible CO<sub>2</sub> adsorption capability, with only a faint CO<sub>2</sub> desorption signal at temperatures below 100 °C (physical absorptions). Due to the weak adsorption capacity of unetched BDD for CO<sub>2</sub>, a carbon-terminal hydrogenation process is more likely to occur, resulting in formate becoming the main product of CO<sub>2</sub> reduction<sup>22,37</sup>. In contrast, after etching, new broad CO<sub>2</sub> desorption bands appear in the 200 °C to 400 °C interval, indicating that the *sp*<sup>2</sup>-C in E-BDDs facilitate CO<sub>2</sub> binding via stronger adsorption modes (chemical absorptions)<sup>43</sup>. Enhancing the CO<sub>2</sub> binding strength would help lower the activation free energy of the reaction and promote the formation of deeply reduced products such as acetate.

For further insights into the possible intermediates and pathways of CO<sub>2</sub> reduction to acetate, in-situ attenuated total reflectance-surface-enhanced infrared absorption spectroscopy (ATR-SEIRAS, details in Methods, Supplementary Fig. 39) were performed on the pristine unetched BDD and E<sub>M</sub>BDD electrodes using CO<sub>2</sub> as the reactant (Supplementary Fig. 40 and Fig. 3b). With the applied potentials from -1.1 to -2 V *vs.* RHE, no obvious absorption peak of \*CO stretching vibration (to CO product) is detected between 1900 and 2100 cm<sup>-1</sup> on the BDD surface (Supplementary Fig. 40), implying that the unetched BDD sample has minimal production and adsorption capacity of CO<sup>44</sup>, which is consistent well with the electrochemical data. However, the distinctive \*OCHO signal, as the primary intermediate for HCOOH<sup>45</sup>, was observed at -1382 cm<sup>-1</sup> on unetched BDD. This observation lends further support to the efficient generation of HCOOH by unetched BDD, which is consistent with the density functional theory (DFT)

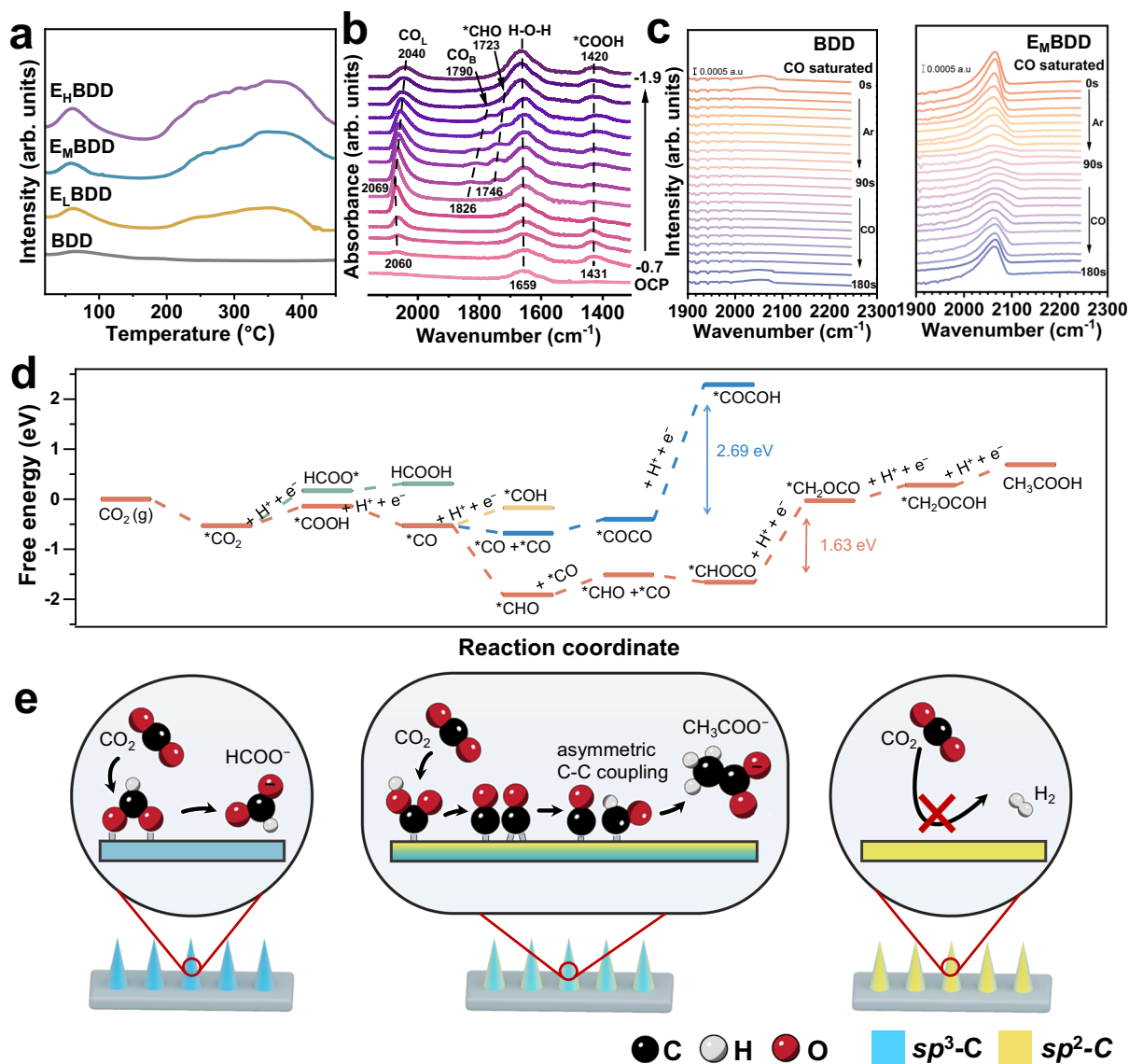


**Fig. 3 | Mechanism investigations of CO<sub>2</sub>RR on BDD and E-BDD.** **a** CO<sub>2</sub>-TPD of BDD, E<sub>L</sub>BDD, E<sub>M</sub>BDD and E<sub>H</sub>BDD. **b** In situ ATR-SEIRAS recorded at different applied potentials for the E<sub>M</sub>BDD in 0.1 M KHCO<sub>3</sub> electrolyte. **c** The infrared spectra under alternating Ar and CO atmospheres. After CO is fully adsorbed ( $t = 0$  s), the gas is switched to Ar, followed by pulsing with Ar-saturated electrolyte. Once the CO signal completely disappears ( $t = 90$  s), the gas is switched back to CO, and pulsing

is performed with CO-saturated electrolyte. **d** Free energy diagram for CO<sub>2</sub> reduction reaction on E-BDD  $sp^3/sp^2$  surface. The orange line shows the more facile way while the green, yellow and blue lines represent the less favorable way. **e** A proposed reaction mechanism for the CO<sub>2</sub>RR to CH<sub>3</sub>COO<sup>-</sup> on different  $sp^3$ -C and  $sp^2$ -C heterostructures. Blue,  $sp^3$  phase; yellow,  $sp^2$  phase; red, oxygen; black, carbon; white, hydrogen. Source data are provided as a Source Data file.

calculation (Supplementary Fig. 41a). In the case of E<sub>M</sub>BDD (Fig. 3b), scanning the applied potential from  $-0.8$  to  $-1.1$  V *vs.* RHE reveals three infrared absorption bands at 2060, 1659, and 1420 cm<sup>-1</sup>, attributed to atop-bounded \*CO<sub>L</sub> (linear) (\*denotes the adsorbed species), the bending mode of H<sub>2</sub>O and \*COOH species, respectively<sup>44,46</sup>. Further scanning to  $-1.2$  V *vs.* RHE, two new bands form at around 1835 and 1746 cm<sup>-1</sup> that could be ascribed to the bridge-bounded \*CO<sub>B</sub> (bridge) and \*CHO species<sup>11,47</sup>. The formation potential of \*CHO matches that of \*CO<sub>B</sub>, suggesting that \*CHO may be formed via hydrogenation of \*CO<sub>B</sub><sup>11</sup>. Additionally, an inverse relationship between the intensity of the \*CO<sub>L</sub> and \*CO<sub>B</sub> peaks was observed. Notably, the intensity of the \*CO<sub>L</sub> peak continuously increased, implying that it is not converted to \*CHO<sup>47,48</sup>. In addition, the intensities of the \*CO<sub>L</sub> and \*CHO bands increased when scanning to more negative potentials ( $-1.3$  V to  $-1.6$  V *vs.* RHE), consistent with the trend of acetate formation. In summary, these suggest the \*CO<sub>L</sub> and \*CHO intermediates play a key role in acetate formation on E<sub>M</sub>BDD. Based on these observations, we

hypothesize a potential mechanism for acetate formation. Initially, CO<sub>2</sub> is reduced to form \*CO<sub>L</sub> and \*CO<sub>B</sub>. Subsequently, \*CO<sub>B</sub> undergoes hydrogenation to form \*CHO, which then couples with other \*CO<sub>L</sub> or \*CHO to produce acetate<sup>12</sup>. However, due to the weaker binding strength of \*CO<sub>L</sub>, it may desorb before reacting, leading to the formation of CO as a byproduct.

Considering the important role of \*CO on acetate formation<sup>10,49</sup>, the binding strength of \*CO on different catalysts was further compared by measuring the desorption rate of \*CO with the ATR-SEIRAS<sup>50</sup>. To estimate the \*CO desorption rate constant, the peak area of linearly bound \*CO near 2060 cm<sup>-1</sup> in the ATR-SEIRAS was monitored at  $-0.5$  V *vs.* RHE, at which no CORR is expected to occur. The CO-saturated electrolyte is first transferred to the reactor. After the CO adsorption equilibrium was established, CO was switched to Ar gas while simultaneously introducing Ar-saturated electrolyte. The IR spectra of adsorbed \*CO on the BDD and E<sub>M</sub>BDD samples were recorded over time (Fig. 3c). In the initial state, the intensity of the \*CO adsorption

band on E<sub>M</sub>BDD is significantly higher than that on BDD, indicating that E<sub>M</sub>BDD possesses a higher adsorption capacity for \*CO. When switching to Ar gas, the adsorbed \*CO band of the BDD decreases rapidly, and the \*CO band could no longer be observed after about 30 s. While the \*CO band of E<sub>M</sub>BDD weakened slowly, reaching its lowest value after 90 s.

In order to obtain an intuitive quantitative comparison, the decay of \*CO coverage over time was tracked by integrating and normalizing the \*CO infrared absorption band areas (Supplementary Fig. 42). At  $t = 0$  s (when catalyst surface was saturated with \*CO), the coverage was defined as the maximum ( $\theta_0 = 1$ ). The \*CO desorption kinetics were analyzed by fitting the data to the first-order rate expression<sup>50</sup>:

$$\theta_t = \theta_0 \exp(-k_d t) \quad (1)$$

where  $k_d$  denotes the \*CO desorption rate constant, while  $\theta_t$  and  $\theta_0$  correspond to the \*CO coverage at any time and  $t = 0$  s, respectively. The derived  $k_d$  values were  $0.017 \text{ s}^{-1}$  for E<sub>M</sub>BDD and  $0.128 \text{ s}^{-1}$  for BDD, indicating a significantly faster \*CO desorption rate on BDD compared to E<sub>M</sub>BDD. These results demonstrate a stronger \*CO binding on the E<sub>M</sub>BDD surface. Moreover, when the atmosphere is switched back to CO, the adsorption peak strength of \*CO gradually returns to the initial state, indicating that the precisely controlled  $sp^2$ -C/ $sp^3$ -C heterostructure of E<sub>M</sub>BDD exhibits a moderately reversible adsorption capability for \*CO. According to the Sabatier principle, this moderate adsorption of \*CO intermediates, which is neither too weak to cause premature desorption nor too strong to poison the surface, is key to the ability of E<sub>M</sub>BDD to selectively produce acetate.

To gain atomic-level insights into the effect of carbon configuration (hybridization), we performed DFT calculations to obtain the free energy diagram for the reaction pathway of CO<sub>2</sub> to HCOOH or CH<sub>3</sub>COOH on diamond ( $sp^3$ ), graphite ( $sp^2$ ), and E-BDD ( $sp^3/sp^2$ ) (Fig. 3d and Supplementary Fig. 41, details in Methods). As revealed by AC-TEM observations, the (101) surface of  $sp^3$ -C was exposed while the  $sp^2$ -C layer grew along the [111] orientation. Therefore, we constructed DFT models to reflect these experimentally observed features. In this configuration, the graphite layer connects to the (101) surface atoms of diamond along the [111] orientation, forming an interface of  $sp^2$ -C and  $sp^3$ -C, while C atoms on the opposite side of graphite were passivated by H atoms to stabilize the framework<sup>31,32</sup> (Supplementary Data 1 and Supplementary Fig. 43c).

Our calculations reveal that E-BDD ( $sp^3/sp^2$ ) exhibits a greater affinity for binding the carbon terminal of CO<sub>2</sub> and converting it to \*CO (Supplementary Figs. 44a and 45), with the lowest reaction energy of  $-0.54 \text{ eV}$  (Fig. 3d and Supplementary Fig. 41). In contrast, the conversion of CO<sub>2</sub> to \*CO is significantly more challenging on the surface of diamond ( $sp^3$ ) or graphite ( $sp^2$ ) (Supplementary Fig. 41b). On the diamond surface, \*CO<sub>2</sub> preferentially binds via the oxygen terminal (Supplementary Fig. 44b), ultimately converting to HCOOH (Supplementary Fig. 41a), as supported by in-situ ATR-SEIRAS results (Supplementary Fig. 40). To demonstrate the subsequent conversion of \*CO, two principal pathways for C<sub>2+</sub> production were evaluated. The first involves direct C–C coupling between two \*CO intermediates to form C<sub>2+</sub> products. The second pathway involves hydrogenation of \*CO, forming either \*CHO or \*COH intermediates, which then undergo C–C coupling. The results indicate that on the E-BDD surface, the \*CHO intermediate is the dominant stable species due to the preferred hydrogenation on the C atom of \*CO (Supplementary Fig. 46). Accordingly, the coupling of \*CO and \*CHO is identified as the predominant route for acetate formation on E-BDD surfaces, consistent with in-situ spectroscopy observations. Bader charge analysis further corroborates this observation, revealing significantly greater charge transfer on carbon atoms upon \*CHO and \*CO dimerization compared to the \*CO-\*CO pathway (Supplementary Fig. 47). We also examined the hydrogenation steps following C–C coupling in the \*CO-\*CO and

\*CHO-\*CO pathways (Fig. 3d). The lowest-energy route for \*CO-\*CO hydrogenation proceeds via \*CO-\*COH formation, but requires overcoming a high free energy barrier of  $2.69 \text{ eV}$ . In contrast, the hydrogenation of the \*CHO-\*CO intermediate has a significantly lower barrier of  $1.63 \text{ eV}$ . Thus, the \*CHO-\*CO pathway is concluded to be the most energetically favorable route for acetate formation.

The data presented above substantiate the assertion that the fabrication of a heterostructure comprising  $sp^2$ -C and  $sp^3$ -C enhances the affinity of the diamond electrode to CO<sub>2</sub> and reaction intermediates, and finally realizes the conversion of CO<sub>2</sub> to acetate (Fig. 3e). Conversely, pure  $sp^3$ -C structure exhibits a weak binding to CO<sub>2</sub>, with the preference for hydrogenation at the carbon terminal, resulting in the formation of formic acid as the primary product. On the other hand, upon introducing the  $sp^2$ -C, the bonding strength of CO<sub>2</sub> and CO on the catalyst surface increases. The adsorbed \*CO<sub>2</sub> is hydrogenated at the oxygen end to form two different \*CO intermediates on E<sub>M</sub>BDD. \*CO<sub>B</sub> is preferentially hydrogenated to form \*CHO, which immediately couples to \*CO<sub>L</sub>. Eventually, the asymmetric \*CO<sub>L</sub>-\*CHO intermediate is converted to acetate by further hydrogenation. Excessive  $sp^2$ -C structure can cover the catalyst surface, leading to masking of  $sp^3$ -C sites, which would weaken the capability of CO<sub>2</sub>RR. Therefore, a moderate  $sp^2$  modification regulates the adsorption balance of key reaction intermediates such as \*CO<sub>2</sub>, CO\*, and \*H, which is key to the formation of acetate.

### The CO<sub>2</sub> capture effect of amino groups

As mentioned above, the amino groups were observed to further enhance the FE of acetate, primarily by facilitating the capture of CO<sub>2</sub> on the catalyst surface. To verify this, we investigated the CO<sub>2</sub> adsorption capacity of E<sub>M</sub>BDD-NH<sub>2</sub> using CO<sub>2</sub>-TPD. Since the specific surface area remained essentially unchanged after amino modification of E<sub>M</sub>BDD, the observed changes in CO<sub>2</sub> desorption behavior should primarily result from the amino functionalization. The intensity of the CO<sub>2</sub> desorption peak below  $100 \text{ }^\circ\text{C}$  remains unchanged (Fig. 4a). However, a significant increase in the intensity of the desorption peak was observed in the high-temperature region ( $200$  to  $400 \text{ }^\circ\text{C}$ ), suggesting that the introduction of the amino group enhances the chemisorption of CO<sub>2</sub>. In addition, blank control experiments were conducted on the E<sub>M</sub>BDD-NH<sub>2</sub>, confirming that the CO<sub>2</sub> signal does not originate from electrode decomposition (Supplementary Fig. 48).

Similarly, ATR-SEIRAS was also used to investigate the CO<sub>2</sub> reduction process on E<sub>M</sub>BDD-NH<sub>2</sub> (Fig. 4b). The observations from ATR-SEIRAS on EMBDD-NH<sub>2</sub> are almost identical to those on E<sub>M</sub>BDD, with the key intermediates (\*COOH, \*CO<sub>L</sub>, \*CO<sub>B</sub>, and \*CHO) for acetate formation remaining consistent. Thus, the pathway of acetate formation remains unaltered, reaffirming that the reaction sites are still  $sp^2$ -C and  $sp^3$ -C heterostructure (Supplementary Fig. 31). Interestingly, a new infrared absorption band of the symmetric N–H deformation vibration in carbamate shifts ( $\delta\text{N-H}$ ,  $1495 \text{ cm}^{-1}$ ) was identified, resulting from the combination of the amino group with CO<sub>2</sub><sup>51</sup>. This observation suggests that the amino group possesses the capacity to capture CO<sub>2</sub>.

We further investigated the impact of amino groups on the adsorption properties of CO and the conversion of CO to acetate by conducting CO desorption tests and CO reduction reactions (Supplementary Fig. 49 and Fig. 4c). Using the same quantification methods mentioned above, the  $k_d$  values are determined as  $0.017 \text{ s}^{-1}$  for E<sub>M</sub>BDD and  $0.018 \text{ s}^{-1}$  for E<sub>M</sub>BDD-NH<sub>2</sub>, indicating that the presence of amino groups on the catalyst surface does not significantly alter the CO adsorption strength. In addition, the effect of aminos on the conversion of CO to acetate was further explored by performing CO reduction on both E<sub>M</sub>BDD and E<sub>M</sub>BDD-NH<sub>2</sub> under different potentials ( $-1.3$  to  $-1.6 \text{ V vs. RHE}$ ) (Fig. 4d). The formation of acetate via CO reduction confirms that the reaction pathway involves an intermediate \*CO species, while the similar acetate yields suggest that the introduction of amino groups does not accelerate the subsequent conversion of

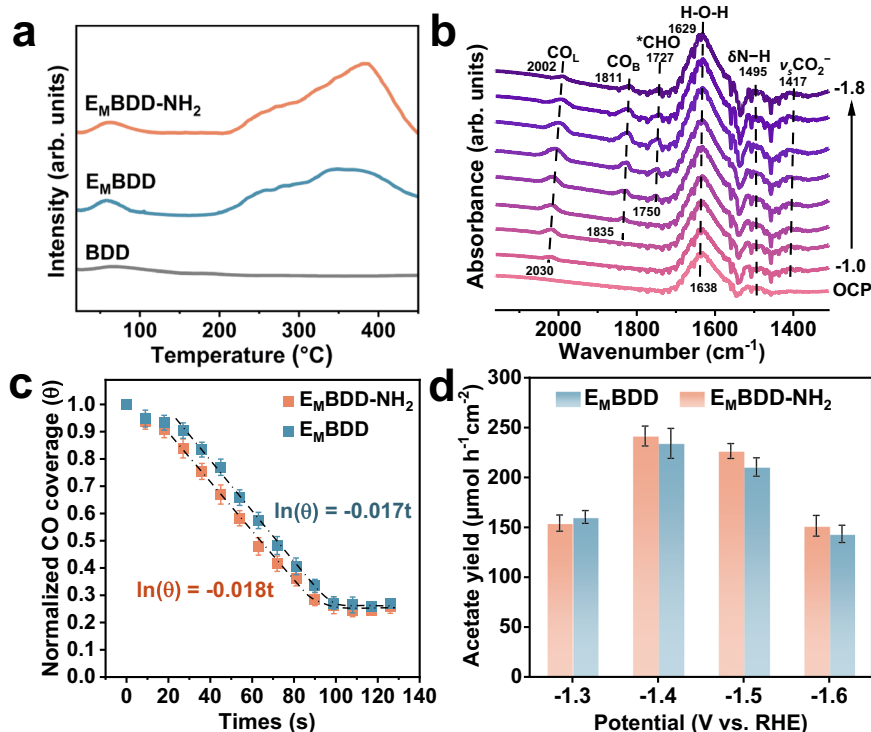


**Fig. 4 | Investigations of the effect of the amino group in facilitating the formation of acetate.** **a** CO<sub>2</sub>-TPD of BDD, E<sub>M</sub>BDD, and E<sub>M</sub>BDD-NH<sub>2</sub>. **b** In situ ATR-SEIRAS recorded at different applied potentials for the E<sub>M</sub>BDD-NH<sub>2</sub> in 0.1 M KHCO<sub>3</sub> electrolyte. **c** Normalized CO coverage obtained from the CO band in ATR-SEIRAS of E<sub>M</sub>BDD and E<sub>M</sub>BDD-NH<sub>2</sub> as a function of time. **d** Acetate yield by CO reduction on

E<sub>M</sub>BDD and E<sub>M</sub>BDD-NH<sub>2</sub> at various applied potentials (*vs.* RHE) in 0.1 M KHCO<sub>3</sub> (pH = 8.52) at room temperature (25 °C) without iR compensation. The error bars represent the standard deviations from at least three independent measurements. Source data are provided as a Source Data file.

\*CO intermediates to acetate. Given these results, it is reasonable to conclude that the observed increase in acetate yield can be mainly attributed to an enhanced capability of the catalyst to capture CO<sub>2</sub>.

## Discussion

In summary, we have devised a deposition-etching strategy for precise control of *sp*<sup>2</sup>-C and *sp*<sup>3</sup>-C heterostructures, effectively modulating the electronic structure and adsorption characteristics at heterogeneous interfaces. CO<sub>2</sub>-TPD and CO desorption kinetics experiment revealed that the introduction of *sp*<sup>2</sup>-C on the surface modifies the adsorption dynamics of key intermediates such as \*CO<sub>2</sub> and \*CO, thus shifting product selectivity from formate to acetate. Spectroscopic analyses and DFT calculations identified \*CO and \*CHO as crucial intermediates in C–C coupling, offering an energetic advantage over other pathways.

To overcome the limitations of mass transfer and the high activation barrier of CO<sub>2</sub>, aminos were introduced to enhance CO<sub>2</sub> adsorption and activation, thereby accelerating acetate formation. Consequently, the E<sub>M</sub>BDD-NH<sub>2</sub> electrode achieved a Faradaic efficiency of 62.7% for acetate and a current density of 23 mA cm<sup>-2</sup> under ambient conditions. Remarkably, the FE for acetate remained above 50% even after over 100 h of durability testing. The exceptional yield and stability of the diamond electrodes can be attributed to their adsorption characteristics and structural integrity. This study marks a significant advancement in developing efficient and durable electrocatalysts for converting CO<sub>2</sub> to acetate.

Nevertheless, significant research efforts remain essential to advance towards future CO<sub>2</sub> refineries. Specifically, compared to CO<sub>2</sub>RR using high-purity CO<sub>2</sub>, utilizing low-concentration CO<sub>2</sub> sources like flue gas offers both greater value and greater challenges. Therefore, future research should focus on the design of novel flow reactor systems, the fabrication of porous and

hydrophobic BDD electrodes, and the development of new surface functionalization groups—all of which are crucial for enhancing gas capture and mass transport rates.

## Methods

### Material

CO<sub>2</sub>, H<sub>2</sub>, Ar, CH<sub>4</sub>, and CO were all supplied by Air Liquide (≥99.999%). C<sub>3</sub>H<sub>8</sub>B (≥99.999%) was purchased from Dalian Special Gas Co., Ltd. KHCO<sub>3</sub> (AR) and KNO<sub>3</sub> (AR), phenol (GC), DMSO (GC), and K<sub>2</sub><sup>13</sup>C<sub>3</sub> (98 atom% <sup>13</sup>C) were purchased from Sigma-Aldrich Industrial Co., Ltd. <sup>13</sup>CO<sub>2</sub> was purchased from Global Rare Gases. The reagents were used without any purification process. Ultra-purity water (18.25 MΩ·cm) supplied by a UP Water Purification System was used in the whole experimental process.

### System configuration

ICP-RIE System Configuration. The custom-designed inductively coupled plasma reactive ion etching (ICP-RIE) system (Supplementary Fig. 1) employs a modular architecture centered around a dielectric-material (quartz) vacuum chamber (12-inch diameter). A height-adjustable two-turn helical copper coil, positioned externally and concentrically aligned with the vacuum chamber axis (Supplementary Fig. 2a and 2b), generates ICP plasma through 13.56 MHz RF supply. A bottom-mounted CCP electrode connected to 13.56 MHz RF supply through a vacuum feedthrough on pedestal enables optimized dual-mode plasma interaction, while the pedestal incorporates double-layer molybdenum heating elements sustaining 1000 °C process temperatures and a tungsten substrate chuck for enhanced etch resistance and thermal conductivity. Process gases are precisely regulated via a precursor manifold with mass flow controllers (MFCs), and then delivered into the chamber through a height-adjustable showerhead injector to ensure uniform gas distribution across the pedestal (Supplementary

Fig. 2a and 2c). Symmetrically arranged subsystems integrate with the core vacuum reaction chamber: one module incorporates control power, vacuum gauges and two tunable RF power supplies (13.56 MHz, 100-1000 W ICP / 0-500 W CCP) coupled to automated impedance matching networks through transmission lines, while the opposing module incorporates a hybrid vacuum system combining Roots pump (1200 L/s) and dry scroll pump, with real-time pressure monitoring via dual-range vacuum gauges ( $10^{-4}$  -  $10^2$  Torr). This configuration achieves independent control of plasma density (via ICP power modulation) and ion bombardment energy (via CCP bias adjustment), enabling the combination of chemical etching reactions with physical bombardment etching, which results in high etch rates, high etch selectivity, and low surface damage.

### Preparation of E<sub>L</sub>BDD, E<sub>M</sub>BDD, and E<sub>H</sub>BDD

The commercially available as-deposited polycrystalline BDD films grown on silicon (100) substrate with the 2.45 GHz MPCVD reactor<sup>22,37</sup>. The diamond powder as seed, (~1 μm, Kemet Corp.) was dispersed in isopropyl alcohol solution with a concentration of 1 mg/ml. To achieve a uniform deposition and highly efficient diamond seeding onto the substrate surface, the silicon wafer (<100>, thickness, ~0.50 mm, resistivity, ~0.001-0.005 Ωcm) was subjected to ultrasonication with diamond seeds slurry for a duration of 1 h. Methane (CH<sub>4</sub>) and trimethylboron (C<sub>3</sub>H<sub>9</sub>B) were used as the carbon and boron sources, respectively. The B/C ratio corresponds to the molar ratio of trimethylborane to methane (1:1000)<sup>52</sup>. The boron doping concentration was ensured to be below 10 ppm to meet electronic grade requirements. The E-BDDs were etched using custom-designed ICP-RIE equipment<sup>29,53</sup> (Supplementary Fig. 1). The ICP-RIE etcher utilizes separate CCP and ICP radio frequency (RF) generators to provide individual control over ion energy and ion density, respectively, enabling a high process flexibility. The plasma was generated by an ICP source radio frequency of 13.65 MHz coupled with a CCP source radio frequency of 13.65 MHz. The base pressure was at 10 mTorr. For E<sub>L</sub>BDD, H<sub>2</sub> and Ar were delivered into the chamber, and the flow rate of H<sub>2</sub> and Ar were 110 sccm and 90 sccm, respectively. During the RIE, the ICP and CCP power were 550 W and 100 W, respectively (details in Supplementary Methods). The showerhead to substrate distance was set to 15 cm and the work pressure was at 0.5 Torr. The molybdenum stage was heated to 300 °C. The etching time was 20 min. For E<sub>M</sub>BDD, the CCP power was set to 200 W, and the etching time was 30 min, other conditions were the same as E<sub>L</sub>BDD. For E<sub>H</sub>BDD, the CCP power was set as 300 W and the etching time was 40 min, other conditions were the same as E<sub>L</sub>BDD.

### Preparation of E<sub>M</sub>BDD-NH<sub>2</sub>

The prepared E<sub>M</sub>BDD electrodes were electrolyzed in 0.5 M KNO<sub>3</sub> electrolyte (pH = 6.87) at -1.5 V vs. RHE for 1 h, with platinum as the counter electrode. A potentiostat (Autolab PGSTAT204, Metrohm) was used for the pre-reduction. Subsequently, the final samples were fabricated.

### Operational parameters

The E-BDD samples were processed in ICP-RIE system<sup>29,53</sup> using H<sub>2</sub>/Ar (110/90 sccm) gas at 0.5 Torr chamber pressure, with the molybdenum pedestal temperature stabilized at 300 °C. For E<sub>L</sub>BDD fabrication, the ICP and CCP powers were set to 550 W and 100 W, respectively, followed by a 20-minute etching process. Subsequent E<sub>M</sub>BDD processing maintained identical gas composition and ICP power while increasing CCP power to 200 W and extending the etching duration to 30 minutes. For E<sub>H</sub>BDD synthesis, the CCP power was further elevated to 300 W with a 40-minute etching period, preserving all other experimental parameters including gas flow rates, chamber pressure, substrate temperature, and ICP power configuration from the E<sub>L</sub>BDD protocol.

The energy density characteristics of the dual plasma source were quantified through two distinct metrics: power density per unit volume ( $\rho_{ICP}$ , W/cm<sup>3</sup>) for the ICP subsystem and power density per unit area ( $\rho_{CCP}$ , W/cm<sup>2</sup>) for the CCP subsystem. For the ICP system, where energy transfer occurs predominantly through the induction coil, the  $\rho_{ICP}$  was calculated as:

$$\rho_{ICP} = \frac{P_{ICP}}{V_{plasma}}$$

where  $P_{ICP}$  represents the RF power input 550 W, and  $V_{plasma}$  denotes the plasma volume (cm<sup>3</sup>) within the 15 cm interelectrode gap between the showerhead and substrate. For the CCP subsystem governing ion acceleration,  $\rho_{CCP}$  was determined by:

$$\rho_{CCP} = \frac{P_{CCP}}{A_{electrode}}$$

where  $P_{CCP}$  is the bias power (100-300 W), and  $A_{electrode}$  corresponds to the substrate electrode area (cm<sup>2</sup>).

Therefore, multidimensional regulation of plasma energy was achieved by independently modulating the power parameters of ICP and CCP. Specifically, the ICP power density ( $\rho_{ICP} = 50.5$  W/cm<sup>3</sup>) sustained a high-density plasma to ensure sufficient radical flux for chemical etching, while CCP power density ( $\rho_{CCP} = 0.137$ - $0.412$  W/cm<sup>2</sup>) regulated ion bombardment energy and rate through bias voltage, controlling the physical sputtering effects. The synergistic modulation of ICP and CCP parameters precisely regulated ion flux ( $\Phi_{ion}$ ) during etching, driving concurrent cleavage of *sp*<sup>3</sup>-hybridized C-C bonds in diamond lattices through controlled ion bombardment and defect-mediated partial *sp*<sup>3</sup>-C to *sp*<sup>2</sup>-C phase transformation during surface reconstruction, as validated by Raman spectra analysis (Fig. 1h). Based on this mechanism, gradient-structured BDD samples were fabricated through controlled ion flux modulation, designated as E<sub>L</sub>BDD (low  $\Phi_{ion}$ ), E<sub>M</sub>BDD (medium  $\Phi_{ion}$ ), and E<sub>H</sub>BDD (high  $\Phi_{ion}$ ).

### Characterizations

Field emission scanning electron microscopy (FESEM) images (Hitachi S-4800) were obtained with an acceleration voltage of 3 kV. Aberration-corrected Transmission electron microscopy (AC-TEM) and high-resolution TEM (HR-TEM) analyses were performed on JEM-ARM300F2 WGP with an acceleration voltage of 300 kV. Aberration-corrected scanning transmission electron microscopy (AC-STEM) micrographs were obtained by employing a HAADF detector (JEM-ARM300F2 FHP). The electron-beam damage to the TEM and STEM specimen was consciously avoided or minimized in the TEM and STEM observations. In low-magnification BF-STEM mode, the electron irradiation dose is relatively low, which does not induce significant damage to the sample. For high-resolution STEM observations, a very low beam current of 50 pA was used to reduce irradiation damage, with a short dwelling time of 0.2 μs. BF, low-angle ADF (LAADF) and HAADF images were obtained by combining 20 frames from acquired series with drift correction (ETA corrector). No noticeable changes in the interface structure were found by comparing these frames, indicating that electron irradiation damage on the interface structure is negligible. The probe convergence angle was set to 25 mrad. The collecting angles of BF and LAADF were set to 6 mrad and 16-62 mrad, respectively. The collecting angle of HAADF was set to 65-200 mrad to eliminate effects of coherent scattering. Electron energy loss spectroscopy (EELS) spectrum was performed using a Quantum ER/965 P electron detector. The multiple linear least squares (MLLS) standards-based quantification tool in DigitalMicrograph was used to generate the carbon distribution. This work was conducted at the Advanced Instrument Analysis and Testing Center, School of Chemical Engineering and Technology, Tianjin University. Plural scattering

correction was enabled to account for variations in the sample thickness. Grazing incidence X-ray diffraction (GIXRD) measurements were performed using a Smartlab 9KW (Japan) X-ray diffractometer with a grazing incidence angle of  $0.2^\circ$ . X-ray photoelectron spectroscopy (XPS) analyses of samples were conducted using a K-Alpha (PHI 1600 ESCA system) XPS spectrometer with an Al K $\alpha$  X-radiation (1486.6 eV). The carbon structure was determined by a confocal LabRAMHR Evolution, Horiba Jobin Yvon Raman microscopy system and the excitation source was a 532 nm laser. For each spectrum, the average of 8 consecutively acquired spectra was calculated with an acquisition time of 10 s per spectrum.

### Ultra-thin cross-section TEM sample preparation

To ensure the sample resolution, a 50 nm Al<sub>2</sub>O<sub>3</sub> protective layer was pre-deposited on the sample via atomic layer deposition (ALD). Then, the sample was protected by FIB-deposited metal (platinum in the FEI-FIB system), and final thinning to accomplish electron transparency was achieved by using an 8 kV ion beam (Supplementary Fig. 5). To eliminate grain overlaps in AC-TEM and AC-STEM imaging, foils ~60 nm thick were prepared using a focused ion beam (FIB, FEI-Helios NanoLab 460HP), followed by a lift-out process to transfer the thin membrane onto a TEM grid with a micromanipulator. The foils were further thinned to ~10 nm using low-energy argon-ion milling (Fischione Model 1040 NanoMill).

### Electrochemical measurements

Electrochemical experiments were conducted using an Autolab PGSTAT204 workstation (Metrohm), which controlled a custom-designed, gas-tight, two-compartment electrochemical cell system fabricated by Gaossunion Co., Ltd. (Supplementary Fig. 13). The counter electrode was a platinum foil, and an Ag/AgCl electrode (saturated KCl, Gaossunion Co., Ltd., Tianjin) served as the reference. The reference electrode (Ag/AgCl) was calibrated in a 0.5 M H<sub>2</sub>SO<sub>4</sub> solution saturated with H<sub>2</sub> for 30 min prior to measurement. A Nafion™ 212 proton exchange membrane (Chemours) separated the counter and working electrodes. The working compartment contained 20 mL of electrolyte in a sealed chamber, enabling the measurement of gaseous products during the test. CO<sub>2</sub> reduction was carried out in a 0.1 M KHCO<sub>3</sub> solution (pH = 8.52, before CO<sub>2</sub> saturation), which was CO<sub>2</sub>-saturated at room temperature (25 °C) and atmospheric pressure (pH = 6.81, after CO<sub>2</sub> saturation). All the electrolytes were prepared on-site before the test. To eliminate residual air in the reservoir, CO<sub>2</sub> (99.999%, Air Liquide Co., Ltd.) was purged into the electrolyte for 30 minutes. The flow rate of the CO<sub>2</sub> gas flowing into the cathode compartment was maintained at 20 sccm by a mass flow controller (MC-Series, Alicat Scientific). Products were quantified after passing 50 C of charge through the cathode, with measurements taken from at least three replicates to obtain an average value with standard deviation. The electrochemical surface area (ECSA) was determined via double-layer capacitance (C<sub>DL</sub>) measurements.

### CO<sub>2</sub> reduction electrolysis and products analysis

The gas products of the CO<sub>2</sub> electrocatalytic reduction were quantified using an online multiple gas chromatography (GC7890B, Agilent Technologies, Inc.). The setup included a thermal conductivity detector (TCD) connected to a MolSieve 5A packed column (Agilent Technologies, Inc.) for H<sub>2</sub> detection, and a flame ionization detector (FID 1) connected to a Porapak Q packed column (Agilent Technologies, Inc.) for CO detection. To enable more sensitive CO detection, a methanizer was installed for FID 1. Additionally, a second flame ionization detector (FID 2), connected to an HP-PLOT Al<sub>2</sub>O<sub>3</sub> capillary column (Agilent Technologies, Inc.), was employed to detect hydrocarbons (C<sub>2</sub>H<sub>4</sub> and C<sub>2</sub>H<sub>6</sub>). Argon was used as the carrier gas during all measurements. Liquid products dissolved in the catholyte were quantified by <sup>1</sup>H Nuclear Magnetic Resonance (<sup>1</sup>H NMR) spectroscopy at 600 MHz

(JEOL ECZ 600 R). 10 mM diluted Dimethyl sulfoxide (DMSO) and 50 mM phenol were added as an internal standard for the identification and quantification of liquid products. Electrochemical impedance spectroscopy (EIS) measurements were performed at the open-circuit potential over a frequency range of 0.1 to 105 Hz. All potentials were not iR corrected. Linear sweep voltammetry (LSV) scans were recorded in CO<sub>2</sub>-saturated 0.1 M KHCO<sub>3</sub> (pH = 6.81), with potentials referenced to the reversible hydrogen electrode (RHE) scale, calculated using the equation:  $E_{(vs. RHE)} = E_{(vs. Ag/AgCl)} + 0.197 V + 0.0591 \times pH$ . During the CO reduction reaction (CORR) experiment, a constant flow of a CO/N<sub>2</sub> mixture (10 sccm CO, 20 sccm N<sub>2</sub>) was introduced into the gas compartment.

### Liquid products quantification

The liquid products were collected from the cathode and anode chambers after electrolysis. <sup>1</sup>H-NMR spectra were acquired using a JEOL ECZ 600 R 600 MHz spectrometer with solvent suppression. Inverse gated decoupling technology is used unless otherwise stated. For <sup>1</sup>H-NMR analysis, 400  $\mu$ L of electrolyte was mixed with 100  $\mu$ L of a solution containing 10 mM DMSO and 50 mM phenol in D<sub>2</sub>O as internal standards. After vortex mixing for 60 seconds to ensure homogeneity, the sample was transferred to a 5 mm NMR tube. Phenol and DMSO were chosen as internal standards because they did not interfere with peaks arising from CO<sub>2</sub> reduction products and are non-volatile, allowing the same standard solution to be used and stored for all product measurements without appreciable change in concentration. Spectra were acquired using a zg30 pulse sequence with a relaxation delay of 5 s and 64 scans. To quantify the reaction products, the area of product peaks to the right of the water peak was compared to the area of the DMSO peak (chemical shift  $\delta = 2.6$  ppm), and the area of product peaks to the left of the water peak was compared to the area of the phenol peak ( $\delta = 7.2$  ppm)<sup>54</sup>. The coulombs required to produce the measured concentration of each product were calculated and divided by the total coulombs passed during chronoamperometry to determine the Faradaic efficiency. To avoid loss of volatile species, all electrolytes containing liquid products were stored at 4 °C. During the 100-h stability test, sampling was performed at 13 time points over 100 h (average interval ~7 h). All experiments were performed with a minimum of three replicates comprising identical, independent electrolysis runs with full sampling and analytical protocols. Error bars quantifying uncertainty in Faradaic efficiency values were derived from these technical replicates (n  $\geq$  3), representing experimental reproducibility across multiple independent measurements.

### Detection limits for CO<sub>2</sub>RR products

Gas products were quantified using online multi-channel gas chromatography (GC), with H<sub>2</sub> analyzed via TCD at an empirical detection limit (LOD) of 10 ppm, and CO via FID at an LOD of 0.1 ppm. Liquid products were collected from the cathode and anode chambers after electrolysis and analyzed by HPLC and <sup>1</sup>H-NMR (Methods in Supporting Information). HPLC with UV-vis detection at 210 nm was employed as one of the quantitative methods, with samples acidified to pH < 3 prior to analysis to sharpen chromatographic peaks and minimize matrix interference from the KHCO<sub>3</sub> electrolyte. For the acetic acid as primary liquid product, through a 7-point calibration curve in 0.1 M KHCO<sub>3</sub>, the empirical detection limit (LOD, S/N  $\geq$  3) was determined as ~10 ppm (0.17 mM), with the reliable quantification range (LOQ, S/N  $\geq$  10) established at 10–500 ppm (0.17–8.33 mM). Cross-validation was performed via <sup>1</sup>H-NMR (JEOL ECZ 600 R 600 MHz) employing an internal standard and 64 scans, targeting the methyl resonance of acetate at  $\delta = 1.91$  ppm. This method achieved enhanced sensitivity with an LOD of ~0.05 mM (3  $\mu$ M/ppm-level), confirming all HPLC-reported acetic acid concentrations exceeded LOQs of both techniques. Critically, no acetic acid signal was detected in blank electrolyte or anolyte controls.

### Analysis of CO<sub>2</sub>RR products

The Faradaic efficiency (FE) for each product was calculated based on the number of electrons required for its formation and the total charge passed, according to the following equation:

$$\text{FE}(\%) = \frac{\text{product moles} \times \text{number of } e^- \text{ needed for conversion}}{\text{moles of } e^- \text{ passed}} \times 100\%$$

For gaseous products:

$$\text{Products moles} = \text{concentration} \times \text{flow rate} / \text{molar volume} \times \text{time}$$

$$\text{moles of } e^- \text{ passed} = \text{current} \times \text{time} / \text{Faraday constant}$$

For liquid products:

$$\text{Products moles} = \text{concentration} \times \text{liquid volume}$$

$$\text{moles of } e^- \text{ passed} = \text{current} \times \text{time} / \text{Faraday constant}$$

### Isotope labeling experiments

For <sup>13</sup>CO<sub>2</sub> reduction, a 0.05 M electrolyte of <sup>13</sup>C-labeled K<sub>2</sub>CO<sub>3</sub> was employed. Pure <sup>13</sup>CO<sub>2</sub> was introduced at 10 sccm for at least 20 minutes to prepare a 0.1 M <sup>13</sup>C-labeled KHCO<sub>3</sub> electrolyte. Prior to testing, the cell was purged with argon to remove impurities. For <sup>1</sup>H-NMR analysis, <sup>13</sup>C-labeled liquid products were analyzed identically to non-labeled CO<sub>2</sub> reduction products, using a diluted DMSO in D<sub>2</sub>O as an internal standard. For acetate detection via MS, the electrolyte was acidified with HCl, and acetic acid was extracted into dichloromethane. The extract was analyzed by gas chromatography-mass spectrometry (GC-MS) using a Trace 1300 GC coupled to an ISQ 7000 single quadrupole MS system equipped with a DB-FFAP capillary column (30 m × 0.32 mm × 0.5 μm).

### ICP-MS analysis

The 0.3283 g sample of the E<sub>M</sub>BDD-NH<sub>2</sub> catalyst was subjected to microwave-assisted acid digestion employing 8 mL aqua regia (HNO<sub>3</sub>: HCl) and 2 mL HF, following a carefully controlled temperature program (120 °C pre-digestion for 30 min; then ramped to 130 °C/3 min hold, 150 °C/3 min hold/10 min hold, 180 °C/3 min hold/30 min hold). After cooling, the digestate was diluted to 25 mL with deionized water for analysis on an Agilent 7800 ICP-MS (the detection limits are ppb level). The results conclusively demonstrate that the total content of detectable transition metal elements specifically associated with potential contamination sources (including Fe, Ni, Cr, and others) is exceptionally low, with all measured levels below 5 ppm. The predominant elements detected were alkali and alkaline earth metals (Ca: 15.676 ppm, K: 14.663 ppm, Na: 10.314 ppm) (Supplementary Table. 1), consistent with environmental background levels and unrelated to the reactor, electrolyte, or counter electrode. This result is consistent with the characterization of XPS/EDS without metal signals, which confirms that the catalytic activity originates from the intrinsic non-metallic active sites of BDD, and excludes metal contamination introduced by equipment or reagents.

### CO<sub>2</sub> temperature-programmed desorption (CO<sub>2</sub>-TPD)

CO<sub>2</sub>-TPD analysis was conducted using a Micromeritics AutoChem II 2920 equipped with a HIDDEN QIC-20 mass spectrometer (MS). To accurately characterize the CO<sub>2</sub> adsorption behavior of the catalyst, the BDD samples (0.9 cm × 3 cm) with dual-side deposition and etching treatment were placed in a quartz U-tube. Prior to analysis, the catalyst underwent pretreatment at 200 °C for 1 h under continuous Ar

flow (30 sccm) to remove moisture and surface contaminants. The system was subsequently cooled to 50 °C under Ar atmosphere, followed by CO<sub>2</sub> adsorption through switching the carrier gas to CO<sub>2</sub> (30 sccm) for saturation exposure. Then, the gas flow was reverted to Ar for 1 h purge to remove physically adsorbed CO<sub>2</sub>. The temperature-programmed desorption was then initiated with a linear heating ramp from 50 °C to 600 °C at 5 °C/min under Ar flow (10 sccm). The desorbed gas component was continuously monitored and recorded using the online MS. The MS signals presented in the TPD profiles were subtracted by the background signal obtained from a blank experiment with an empty U-tube under identical conditions.

### In-situ ATR-SEIRAS measurements

Au nanofilms were directly deposited on the reflecting plane of a Si prism through a modified electroless chemical deposition technique described by Xu et al.<sup>55</sup> The spectroelectrochemical cell was produced by Gaossunion Co., Ltd., Tianjin, according to the design of Xu et al.<sup>56</sup> (Supplementary Fig. 39b). The Pt counter electrode was separated from the catalyst film working electrode and the saturated Ag/AgCl reference electrode by a piece of proton exchange membrane (Nafion™ 212, Chemours) and 0.1 M KHCO<sub>3</sub> was used as the electrolyte. The electrochemical cell was integrated into a Fourier-transform infrared (FTIR) spectrometer (is50, Nicolet) using a modified accessory set at a 60° angle of incidence (VeeMax III, PIKE Technology) (Supplementary Fig. 39a). All the spectra were recorded with a resolution of 4 cm<sup>-1</sup>. Absorption spectra are presented with positive peaks indicating an increase in signal and negative peaks indicating a decrease in signal. BDD, E<sub>M</sub>BDD, and E<sub>M</sub>BDD-NH<sub>2</sub> were deposited onto Au nano-coated Si prisms as previously described. For each electrode, a background measurement was made at +0.1 V vs. RHE in the Ar-saturated electrolyte. Electrochemical measurements were conducted with a potentiostat (CompactStat.e20250, IVIUM).

### Computational details

All the spin-polarized DFT calculations were performed with the Vienna Ab initio Simulation Package (VASP, 5.4.4 version)<sup>57</sup> under the framework of projector augmented wave method<sup>58,59</sup>. The generalized gradient approximation (GGA) of the Perdew-Burke-Ernzerhof (PBE) functional was employed as the exchange-correlation functional<sup>60</sup>. The valence wave functions were expanded by plane wave with a cutoff energy of 400 eV, while all the structures were optimized until the force on each atom was less than 0.02 eV Å<sup>-1</sup>. 2 × 2 (101) surface model of diamond was constructed to represent sp<sup>3</sup>-C while sp<sup>2</sup>-C was represented by 2 × 2 graphite layer (Supplementary Fig. 43a and b). For the sp<sup>2</sup>-sp<sup>3</sup> hybrid model, the 2 × 2 graphene layer was optimized on the surface of diamond<sup>31,32</sup> (Supplementary Fig. 43c). Notably, these computational results align with our experimental observations from AC-TEM images. Gibbs energy of gas phase CO<sub>2</sub> (g), H<sub>2</sub> (g) and H<sub>2</sub>O (g) were used as the references for the calculation of potential energy diagram, which was optimized in a 25 Å × 25 Å × 25 Å unit cell. The conclusions drawn from our DFT calculations, while providing valuable mechanistic insights, should be interpreted with caution. The computational models represent simplified, static systems that may not fully capture the complexity of the actual catalytic material under operating conditions, including dynamic surface reconstructions, solvent effects, and varying coverages. Therefore, the DFT results are viewed as providing supportive guidance and plausible reaction pathways.

### Data availability

Source data are provided with this paper. Figures 1a and 3e were created with SOLIDWORKS 3D CAD, 3ds Max, VESTA, and Adobe Illustrator CC, all confirmed for commercial publication. Any additional information relating to this study are available from the corresponding author upon reasonable request. Source data are provided with this paper.

## References

1. De Luna, P. et al. What would it take for renewably powered electrosynthesis to displace petrochemical processes? *Science* **364**, eaav3506 (2019).
2. Olah, G. A., Prakash, G. K. & Goeppert, A. Anthropogenic chemical carbon cycle for a sustainable future. *J. Am. Chem. Soc.* **133**, 12881–12898 (2011).
3. Gao, D., Li, W., Wang, H., Wang, G. & Cai, R. Heterogeneous catalysis for CO<sub>2</sub> conversion into chemicals and fuels. *Trans. Tianjin Univ.* **28**, 245–264 (2022).
4. Xia, C. et al. General synthesis of single-atom catalysts with high metal loading using graphene quantum dots. *Nat. Chem.* **13**, 887–894 (2021).
5. Xiao, L. et al. Pd-intercalated black phosphorus: An efficient electrocatalyst for CO<sub>2</sub> reduction. *Sci. Adv.* **10**, eadn2707 (2024).
6. Li, F. et al. Molecular tuning of CO<sub>2</sub>-to-ethylene conversion. *Nature* **577**, 509–513 (2020).
7. Fan, L. et al. Strategies in catalysts and electrolyzer design for electrochemical CO<sub>2</sub> reduction toward C<sub>2+</sub> products. *Sci. Adv.* **6**, eaay3111 (2020).
8. Wei, P. et al. Coverage-driven selectivity switch from ethylene to acetate in high-rate CO<sub>2</sub>/CO electrolysis. *Nat. Nanotechnol.* **18**, 299–306 (2023).
9. Zhu, H. L. et al. Continuously producing highly concentrated and pure acetic acid aqueous solution via direct electroreduction of CO<sub>2</sub>. *J. Am. Chem. Soc.* **146**, 1144–1152 (2024).
10. Jin, J. et al. Constrained C<sub>2</sub> adsorbate orientation enables CO-to-acetate electroreduction. *Nature* **617**, 724–729 (2023).
11. Wang, Y. et al. Amino-functionalized Cu for efficient electrochemical reduction of CO to acetate. *ACS Catal.* **13**, 3532–3540 (2023).
12. Shen, H. et al. Asymmetrical C–C coupling for electroreduction of CO on bimetallic Cu–Pd catalysts. *ACS Catal.* **12**, 5275–5283 (2022).
13. Hammer, B. & Norskov, J. K. Why gold is the noblest of all the metals. *Nature* **376**, 238–240 (1995).
14. Seh, Z. W. et al. Combining theory and experiment in electrocatalysis: Insights into materials design. *Science* **355**, eaad4998 (2017).
15. Zhang, J. et al. Molecular tuning for electrochemical CO<sub>2</sub> reduction. *Joule* **7**, 1700–1744 (2023).
16. Huang, J. E. et al. CO<sub>2</sub> electrolysis to multicarbon products in strong acid. *Science* **372**, 1074–1078 (2021).
17. Zhang, J. et al. Surface chemistry and catalytic reactivity of a nanodiamond in the steam-free dehydrogenation of ethylbenzene. *Angew. Chem. Int. Ed.* **49**, 8640–8644 (2010).
18. Vasileff, A., Zheng, Y. & Qiao, S. Z. Carbon solving carbon's problems: Recent progress of nanostructured carbon-based catalysts for the electrochemical reduction of CO<sub>2</sub>. *Adv. Energy Mater.* **7**, 1700759 (2017).
19. Liu, B. et al. Nanostructured and boron-doped diamond as an electrocatalyst for nitrogen fixation. *ACS Energy Lett.* **5**, 2590–2596 (2020).
20. Wang, H. et al. Synergistic enhancement of electrocatalytic CO<sub>2</sub> reduction to C<sub>2</sub> oxygenates at nitrogen-doped nanodiamonds/Cu interface. *Nat. Nanotechnol.* **15**, 131–137 (2020).
21. Liu, Y., Chen, S., Quan, X. & Yu, H. Efficient electrochemical reduction of carbon dioxide to acetate on nitrogen-doped nanodiamond. *J. Am. Chem. Soc.* **137**, 11631–11636 (2015).
22. Xu, J., Yokota, Y., Wong, R. A., Kim, Y. & Einaga, Y. Unusual electrochemical properties of low-doped boron-doped diamond electrodes containing sp<sup>2</sup> carbon. *J. Am. Chem. Soc.* **142**, 2310–2316 (2020).
23. Natsui, K., Iwakawa, H., Ikemiya, N., Nakata, K. & Einaga, Y. Stable and highly efficient electrochemical production of formic acid from carbon dioxide using diamond electrodes. *Angew. Chem. Int. Ed.* **57**, 2639–2643 (2018).
24. Duan, X. et al. sp<sup>2</sup>/sp<sup>3</sup> framework from diamond nanocrystals: a key bridge of carbonaceous structure to carbocatalysis. *ACS Catal.* **9**, 7494–7519 (2019).
25. Liu, T., Ali, S., Li, B. & Su, D. S. Revealing the role of sp<sup>2</sup>@sp<sup>3</sup> structure of nanodiamond in direct dehydrogenation: insight from DFT study. *ACS Catal.* **7**, 3779–3785 (2017).
26. Lin, Y., Sun, X., Su, D. S., Centi, G. & Perathoner, S. Catalysis by hybrid sp<sup>2</sup>/sp<sup>3</sup> nanodiamonds and their role in the design of advanced nanocarbon materials. *Chem. Soc. Rev.* **47**, 8438–8473 (2018).
27. Zhang, Z. et al. Steering carbon hybridization state in carbon-based metal-free catalysts for selective and durable CO<sub>2</sub> electroreduction. *ACS Catal.* **12**, 15218–15229 (2022).
28. Zhang, J., Xia, Z. & Dai, L. Carbon-based electrocatalysts for advanced energy conversion and storage. *Sci. Adv.* **1**, e1500564 (2015).
29. Banerjee, A. et al. Ultralarge elastic deformation of nanoscale diamond. *Science* **360**, 300–302 (2018).
30. Subramanian, P. et al. Atomic force microscopic and Raman investigation of boron-doped diamond nanowire electrodes and their activity toward oxygen reduction. *J. Phys. Chem. C.* **121**, 3397–3403 (2017).
31. Németh, P. et al. Complex nanostructures in diamond. *Nat. Mater.* **19**, 1126–1131 (2020).
32. Luo, K. et al. Coherent interfaces govern direct transformation from graphite to diamond. *Nature* **607**, 486–491 (2022).
33. Osswald, S., Yushin, G., Mochalin, V., Kucheyev, S. O. & Gogotsi, Y. Control of sp<sup>2</sup>/sp<sup>3</sup> carbon ratio and surface chemistry of nanodiamond powders by selective oxidation in air. *J. Am. Chem. Soc.* **128**, 11635–11642 (2006).
34. Németh, P. et al. Diamond-graphene composite nanostructures. *Nano Lett.* **20**, 3611–3619 (2020).
35. Nomura, Y. et al. Dynamic imaging of lithium in solid-state batteries by operando electron energy-loss spectroscopy with sparse coding. *Nat. Commun.* **11**, 2824 (2020).
36. Mochalin, V. N., Shenderova, O. A., Ho, D. & Gogotsi, Y. The properties and applications of nanodiamonds. *Nat. Nanotechnol.* **7**, 11–23 (2011).
37. Tomisaki, M., Kasahara, S., Natsui, K., Ikemiya, N. & Einaga, Y. Switchable product selectivity in the electrochemical reduction of carbon dioxide using boron-doped diamond electrodes. *J. Am. Chem. Soc.* **141**, 7414–7420 (2019).
38. Asai, M. et al. Marked adsorption irreversibility of graphitic nanoribbons for CO<sub>2</sub> and H<sub>2</sub>O. *J. Am. Chem. Soc.* **133**, 14880–14883 (2011).
39. Takeuchi, K. et al. Adsorption of CO<sub>2</sub> on graphene: a combined TPD, XPS, and vdW-DF study. *J. Phys. Chem. C.* **121**, 2807–2814 (2017).
40. Mikami, T., Yamamoto, T., Tomisaki, M. & Einaga, Y. Amine-functionalized diamond electrode for boosting CO<sub>2</sub> reduction to CO. *ACS Sustain. Chem. Eng.* **10**, 14685–14692 (2022).
41. Xiao, Y. C. et al. Reactive capture of CO<sub>2</sub> via amino acid. *Nat. Commun.* **15**, 7849 (2024).
42. Rooney, C. L., Sun, Q., Shang, B. & Wang, H. Electrocatalytic reductive amination of aldehydes and ketones with aqueous nitrite. *J. Am. Chem. Soc.* **147**, 9378–9385 (2025).
43. Marchon, B., Carrazza, J., Heinemann, H. & Somorjai, G. A. TPD and XPS studies of O<sub>2</sub>, CO<sub>2</sub>, and H<sub>2</sub>O adsorption on clean polycrystalline graphite. *Carbon* **26**, 507–514 (1988).
44. Zhang, G. et al. Selective CO<sub>2</sub> electroreduction to methanol via enhanced oxygen bonding. *Nat. Commun.* **13**, 7768 (2022).
45. Shen, H. et al. Acidic CO<sub>2</sub>-to-HCOOH electrolysis with industrial-level current on phase engineered tin sulfide. *Nat. Commun.* **14**, 2843 (2023).
46. Liang, S. et al. Sulfur changes the electrochemical CO<sub>2</sub> reduction pathway over Cu electrocatalysts. *Angew. Chem. Int. Ed.* **62**, e202310740 (2023).

47. Ma, W. et al. Electrocatalytic reduction of CO<sub>2</sub> to ethylene and ethanol through hydrogen-assisted C–C coupling over fluorine-modified copper. *Nat. Catal.* **3**, 478–487 (2020).
48. Jiang, G. et al. Rational manipulation of intermediates on copper for CO<sub>2</sub> electroreduction toward multicarbon products. *Trans. Tianjin Univ.* **28**, 265–291 (2022).
49. Ji, Y. et al. Selective CO-to-acetate electroreduction via intermediate adsorption tuning on ordered Cu-Pd sites. *Nat. Catal.* **5**, 251–258 (2022).
50. Li, J. et al. Weak CO binding sites induced by Cu-Ag interfaces promote CO electroreduction to multi-carbon liquid products. *Nat. Commun.* **14**, 698 (2023).
51. Danon, A., Stair, P. C. & Weitz, E. FTIR study of CO<sub>2</sub> adsorption on amine-grafted SBA-15: elucidation of adsorbed species. *J. Phys. Chem. C.* **115**, 11540–11549 (2011).
52. Du, J. et al. A new pathway for CO<sub>2</sub> reduction relying on the self-activation mechanism of boron-doped diamond cathode. *JACS Au* **2**, 1375–1382 (2022).
53. Wang, C. et al. Decoupled etch selectivity and optical transparency in controlled deposition of diamond-like carbon films via a reverse antenna PECVD for hard masks. *Sci. China Chem.* <https://doi.org/10.1007/s11426-025-2746-y> (2025).
54. Kuhl, K. P., Cave, E. R., Abram, D. N. & Jaramillo, T. F. New insights into the electrochemical reduction of carbon dioxide on metallic copper surfaces. *Energy Environ. Sci.* **5**, 7050–7059 (2012).
55. Dunwell, M. et al. The central role of bicarbonate in the electrochemical reduction of carbon dioxide on gold. *J. Am. Chem. Soc.* **139**, 3774–3783 (2017).
56. Li, J. et al. Electrokinetic and in situ spectroscopic investigations of CO electrochemical reduction on copper. *Nat. Commun.* **12**, 3264 (2021).
57. Kresse, G. & Furthmüller, J. Efficient iterative schemes for ab initio total-energy calculations using a plane-wave basis set. *Phys. Rev. B* **54**, 11169–11186 (1996).
58. Kresse, G. & Joubert, D. From ultrasoft pseudopotentials to the projector augmented-wave method. *Phys. Rev. B* **59**, 1758–1775 (1999).
59. Grimme, S., Antony, J., Ehrlich, S. & Krieg, H. A consistent and accurate ab initio parametrization of density functional dispersion correction (DFT-D) for the 94 elements H-Pu. *J. Chem. Phys.* **132**, 154104 (2010).
60. Perdew, J. P., Burke, K. & Ernzerhof, M. Generalized gradient approximation made simple. *Phys. Rev. Lett.* **77**, 3865–3868 (1996).

## Acknowledgements

We acknowledge the National Key R&D Program of China (2021YFA1500804), the National Natural Science Foundation of China (22121004, 22038009, and 22250008), Haihe Laboratory of Sustainable Chemical Transformations, the Program of Introducing Talents of Discipline to Universities (No. BP0618007), the Xplorer Prize for financial support.

## Author contributions

J.L.G. and T.W. supervised the project. J.L.G., T.W., and C.J.W. conceptualized the project. T.W., G.Z., C.J.W., and Y.X.W. designed and built equipment. C.J.W. synthesized catalysts. C.J.W. conducted the catalytic tests and the related data processing. G.Z. and M.M.Z. assisted with in-situ ATR-SEIRAS measurements and related data analyses. R.L., X.M., X.C., and Z.-J.Z. carried out the theoretical calculations. C.J.W., T.W., and J.L.G. wrote the manuscript. All authors discussed the results and commented on the paper.

## Competing interests

The authors declare no competing interests.

## Additional information

**Supplementary information** The online version contains supplementary material available at <https://doi.org/10.1038/s41467-025-65504-6>.

**Correspondence** and requests for materials should be addressed to Zhi-Jian Zhao, Tuo Wang or Jinlong Gong.

**Peer review information** *Nature Communications* thanks Biaobiao Zhang and the other anonymous reviewer(s) for their contribution to the peer review of this work. A peer review file is available.

**Reprints and permissions information** is available at <http://www.nature.com/reprints>

**Publisher's note** Springer Nature remains neutral with regard to jurisdictional claims in published maps and institutional affiliations.

**Open Access** This article is licensed under a Creative Commons Attribution-NonCommercial-NoDerivatives 4.0 International License, which permits any non-commercial use, sharing, distribution and reproduction in any medium or format, as long as you give appropriate credit to the original author(s) and the source, provide a link to the Creative Commons licence, and indicate if you modified the licensed material. You do not have permission under this licence to share adapted material derived from this article or parts of it. The images or other third party material in this article are included in the article's Creative Commons licence, unless indicated otherwise in a credit line to the material. If material is not included in the article's Creative Commons licence and your intended use is not permitted by statutory regulation or exceeds the permitted use, you will need to obtain permission directly from the copyright holder. To view a copy of this licence, visit <http://creativecommons.org/licenses/by-nc-nd/4.0/>.

© The Author(s) 2025